CHEMISTRY OF MATERIALS
Cite This: Chem. Mater. 2018, 30, 8211−8220
Article
pubs.acs.org/cm

Fashioning Fluorous Organic Spacers for Tunable and Stable Layered Hybrid Perovskites

Inés García-Benito,[†] Claudio Quarti,[‡] Valentin I. E. Queloz,[†] Simonetta Orlandi,[§] Iwan Zimmermann,[†] Marco Cavazzini,[§] Andreas Lesch,[∥] Sergio Marras,[⊥] David Beljonne,[‡] Gianluca Pozzi,[§] Mohammad Khaja Nazeeruddin,[†] and Giulia Grancini*[,†]

[†]Group for Molecular Engineering of Functional Materials, Institute of Chemical Sciences and Engineering, EPFL Valais Wallis, Rue de l'Industrie 17, CP 440, CH-1951 Sion, Switzerland

[‡]Laboratory for Chemistry of Novel Materials, University of Mons, Place du Parc 20, B-7000 Mons, Belgium

[§]Istituto di Scienze e Tecnologie Molecolari del CNR, ISTM-CNR, via Golgi, 19, I-20133 Milano, Italy

[∥]Laboratory of Physical and Analytical Electrochemistry, EPFL Valais Wallis, Rue de l'Industrie 17, CP 440, CH-1951 Sion, Switzerland

[⊥]Istituto Italiano di Tecnologia (IIT), Via Morego 30, 16163 Genova, Italy

Supporting Information

ABSTRACT: Two dimensional (2D) organic−inorganic hybrid perovskites have recently attracted enormous attention due to their higher environmental stability with respect to three-dimensional (3D) perovskites and larger structural tunability. The layered structure relaxes constraints on the dimensions of the organic cations that alternate the inorganic sheets, opening up a large choice on the organics, ultimately enabling the creation of tunable layered perovskites. Here, we report on a series of fluorous cations, varying in size and shape, as building blocks for a new family of fluorous 2D lead-iodide perovskites. These display a large tunability in the optical and dielectric properties depending on the structure of the fluorous cations. Importantly, despite the invariant inorganic framework, the 2D perovskite electronic structure is strongly affected by the cation size. The longer the cation, the smaller the 2D perovskite band gap and the exciton binding energy (reducing from 400 meV down to 130 meV). Such variation is induced by the strain in the inorganic sheet, resulting in a more dispersed valence and conduction bands, in turn yielding a smaller band gap. In addition, a smaller effective mass for the 2D perovskite with the longest cation is calculated, for which improved transport properties are anticipated. Importantly, the fluorous moiety confers extreme stability to the 2D perovskite and enhances the hydrophobic character of the perovskite surface, which remains perfectly stable for more than one month in ambient conditions.

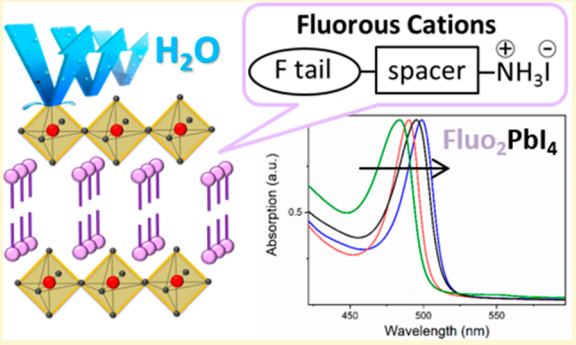

INTRODUCTION

In the last decades, hybrid perovskites (HPs) in the form of three-dimensional (3D) structures, have retained much attention in the optoelectronic sector.[1−4] HP-based photovoltaics, in particular, has witnessed an incredible boom, with solar to electricity power conversion efficiency (PCE) nowadays beyond 23% and comparable to commercially available solar technologies.[5,6] However, the full potential of this technology and the big excitement that came along have been recently questioned by their relatively poor stability upon exposure to air, which affects perovskite based-devices under operative conditions.[7] By contrast, their parent low dimensional perovskites arranging in the 2D, so-called *Ruddlesden−Popper*-phase, have demonstrated higher environmental stability,[8,9] paving the way for their possible integration in working devices as a "stabilizer" component.[10] 2D HPs can be structurally obtained by slicing the 3D frameworks along the inorganic crystallographic planes. The structure reads as R_2BX_4 where R is an organic molecule (such as an aliphatic or aromatic alkylammonium cation, that is, 2-phenylethylammonium or *n*-butylammonium) acting as a spacer between the inorganic layers; B the divalent metal and X the halogen atom.[11] This results in single inorganic sheets (n = 1, n = number of inorganic planes), sandwiched in between the organic cation layers. Notably, the layered structure relaxes the limit imposed on the size of the organic cation by the known *Goldschmidt tolerance factor* that exists for the 3D perovskites, since the organic cation must no longer fit in the voids of the octahedra.[12] A wide library of organic cations becomes therefore available. Due to the reduced dimensionality, 2D

Received: August 8, 2018
Revised: October 23, 2018
Published: October 24, 2018

DOI: 10.1021/acs.chemmater.8b03377
Chem. Mater. 2018, 30, 8211−8220

Scheme 1. Synthesis of Ammonium Salts[a]

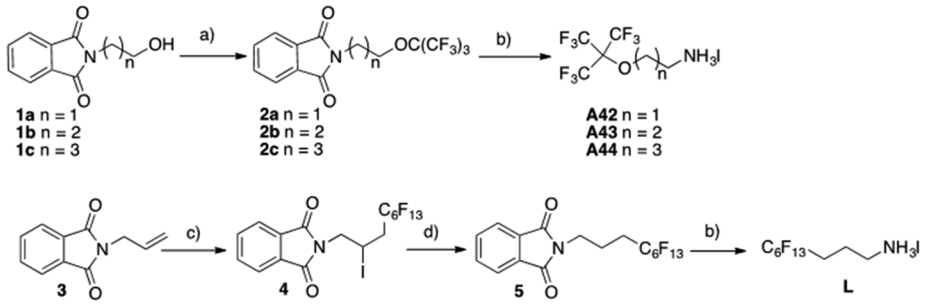

[a](a) Perfluoro-*tert*-butanol, PPh_3, DIAD, Et_2O, 0°C to RT; (b) NH_2NH_2, MeOH, reflux, then HI_{aq}, RT; (c) $C_6F_{13}I$, Zn, CH_2Cl_2, RT; (d) H_2 (4 atm), Pd/C, TEA, THF, RT.

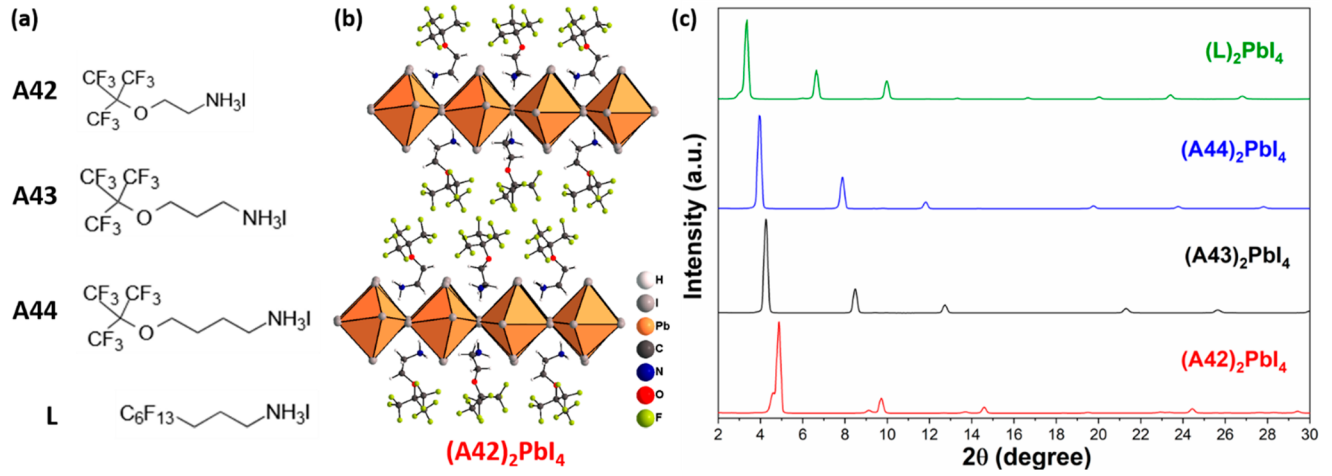

Figure 1. (a) Molecular structure and abbreviated name of the studied fluorous cations. (b) Schematic structure of 2D HP with **A42** as the organic spacer between the inorganic PbI_6 layer. (c) Out of plane X-ray diffraction (XRD) patterns of the $(\mathbf{A42})_2\mathbf{PbI_4}$, $(\mathbf{A43})_2\mathbf{PbI_4}$, $(\mathbf{A44})_2\mathbf{PbI_4}$, and $(\mathbf{L})_2\mathbf{PbI_4}$ in thin films.

HPs possess a larger band gap, usually in the range of 2.2−2.9 eV.[11,13] Dielectric mismatch and low dielectric screening from the organic layer induce the stabilization of strongly localized excitons,[14] with binding energies generally in the order of hundreds meV,[11,13,15−17] along with a large oscillator strength.[18] Thus, pronounced excitonic effects have been typically reported[19] such as photo and electro-luminescence,[20,21] biexciton lasing,[22] and large third-order optical nonlinearities.[23] Notably, the exciton confinement and band gap can be tuned by the different organic barriers changing the dielectric properties of the quantum well.[24,25] In addition, changing the barrier layer can also result in a structural distortion of the inorganic framework.[26] In-plane distortion, for instance, can increase the charge density and reduce the wave function overlap within the inorganic layer, ultimately affecting the bandwidth of the valence and conduction bands, and the band gap of the 2D HPs.[27,28]

In this work, we synthesize a new family of fluorous ammonium cations as organic spacers to create new stable 2D HP. Fluorous compounds are characterized by the presence of highly fluorinated, saturated molecular fragments, usually linear medium sized perfluoroalkyl chains.[29] They show distinct properties compared to their fully hydrocarbon-, mono/polyfluorinated-, or trifluoromethylated analogues. In particular, their simultaneously hydrophobic and lipophobic behavior is utilized in a variety of applications, spanning from catalysis to medicine.[30] Whereas 2D HPs featuring fluorinated alkyl or aryl ammonium cations as organic spacers have been previously proposed[31−34] (i.e., using 2-fluoroethylammonium ($FC_2H_4NH_3^+$)),[35] perovskite materials incorporating fluorous ammonium are virtually unknown. The presence of the fluorous cations in the resulting 2D perovskite can impart an additional water-repellent character and superior stability with respect to fully hydrocarbon-based cations used so far.[36] In this work, we design four new fluorous ammonium cations having different shapes, that is, from branched to linear, fluorine loading, and length (varying the alkylene spacer) used to develop stable fluorous 2D HPs thin films with remarkable hydrophobic character. We observe that the systematic modification of the fluorous cations dimension and molecular structure impacts on the optoelectronic properties of the 2D HPs. The length of the cation tunes those properties that are paramount for optoelectronic device optimization such as the band gap and exciton binding energies, which varies from 420 to 130 meV.[11,37] In addition, the longest cation boosts the thin film water-repellent character leading to a superior hydrophobicity with respect to standard 3D hybrid perovskite.[38,39] The fluorous 2D HPs exhibit a remarkably high moisture resistance, that kept intact their structural and optical properties upon aging for one month in ambient atmosphere (RH = 40%).

DOI: 10.1021/acs.chemmater.8b03377
Chem. Mater. 2018, 30, 8211−8220

Table 1. Theoretical Lattice Parameters of $(A42)_2PbI_4$, $(A43)_2PbI_4$, $(A44)_2PbI_4$ and $(L)_2PbI_4$

2D HPs	$(A42)_2PbI_4$		$(A43)_2PbI_4$		$(A44)_2PbI_4$		$(L)_2PbI_4$	
space group	monoclinic		triclinic		monoclinic		monoclinic	
lattice parameters	a = 8.932	α = 90.00	a = 8.869	α = 89.16	a = 8.829	α = 90.00	a = 9.021	α = 90.00
	b = 8.564	β = 77.77	b = 8.871	β = 78.72	b = 8.821	β = 78.95	b = 8.695	β = 72.22
	c = 18.886	γ = 90.00	c = 21.202	γ = 88.25	c = 23.017	γ = 90.00	c = 20.390	γ = 90.00

RESULTS AND DISCUSSION

Synthesis of Fluorous Cations and Preparation of 2D HPs. We designed a series of primary ammonium iodides sharing a common three-block, perfluoroalkyl tail-alkylene linker-$NH_3^+I^-$, structure. Within this basic arrangement, variations in the nature of the fluorinated tail and linker allows us to obtain cationic moieties of different molecular length, cross sectional area, and rigidity. The fluorous ammonium salts were obtained through straightforward synthetic elaborations of commercially available perfluoroalkylated building-blocks. The set of fluorous ammonium iodides **A4n** characterized by the presence of the nonafluoro-*tert*-butyloxy tail were prepared using a two-step procedure based on Rábai's synthesis of branched fluorous amines (Scheme 1).[40] In brief, condensation under Mitsunobu conditions of the readily available (*N*-hydroxyalkyl)amino phthalimide derivatives **1a−c** with perfluoro-*tert*-butanol afforded the corresponding perfluoro-*tert*-butyl ethers **2a−c**, from which the **A4n** salts were released by hydrazinolysis followed by acidic workup in the presence of aqueous hydrogen iodide. The linear alkyl ammonium salt **L** containing a *n*-perfluorohexyl unit was likewise prepared by hydrazinolysis of a phthalimide derivative obtained via a different route, also shown in Scheme 1. In this case, the masked amine **5** was obtained by addition of perfluorohexyl iodide to *N*-allyl phthalimide **3** in the presence of zinc, followed by dehalogenation of intermediate **4**. Deprotection of **5** by reaction with hydrazine in refluxing methanol and subsequent treatment with aqueous hydrogen iodide afforded the desired ammonium salt. For the sake of simplicity, hereafter we classify them in two categories: the branched family, consisting of a fluorinated ending group and ammonium moiety separated by an ethylene, propylene or butylene group, named **A42**, **A43**, and **A44**, respectively, and the linear cation, **L**, consisting of six carbon atoms in the linear fluorous tail and three $-CH_2$ units inserted between the fluorous tail and the NH_3^+ head (Scheme 1 and Figure 1a).

The **A42**, **A43**, **A44**, and **L**-based **PbI_4**-2D HPs were obtained in the form of thin films and single crystals. For thin films, the precursor solutions were prepared by mixing a 2:1 molar ratio of the corresponding cation and PbI_2 in DMSO. Different conditions for the film deposition were examined to improve the film quality, varying composition ratios of the precursors, treatments of the substrates (cleaning treating, hot-casting)[41] and antisolvents (chlorobenzene, toluene, trifluorotoluene).[42,43] In our case, the use of an one-step deposition method with chlorobenzene as antisolvent provided the best protocol to obtain smooth thin films, along with annealing at 100 °C for 10 min (see top view morphology from scanning electron microscope images in Supporting Information (SI) Figure S1). On the other hand, single crystals were obtained by heating stoichiometric amounts of the organic cations and lead iodide in hydriodic acid at a concentration of ∼0.1 M at 100 °C for 1 day (see SI for further details). As a result, the newly synthesized cations infiltrate in between the inorganic PbI_6 layers, forming a pure 2D HP (n = 1), as shown in Figure 1b for the **$(A42)_2PbI_4$**.

Structural and Optical Characterization of 2D HPs. The crystalline structure at room temperature of our new fluorous 2D HPs has been unveiled by combining X-ray diffraction (XRD) analyses on both thin films and single crystal. The investigated thin films display an XRD pattern rich in the low angle region, as shown in Figure 1c, indicative of a n = 1 2D HP structure.[11,13,44] More in details, the patterns are dominated by the equally spaced (00l) reflections, peaking at 4.9°, 4.3°, 3.9°, and 3.4° for **$(A42)_2PbI_4$**, **$(A43)_2PbI_4$**, **$(A44)_2PbI_4$**, and **$(L)_2PbI_4$**, respectively. The shift of the peak is due to the larger distance between the inorganic planes, as the cation size increases. The reflections of the other (*hkl*) planes are strongly suppressed, confirming the remarkable preferred orientation of the inorganic planes, aligning parallel to the substrate.[11,44] From those reflections, we can calculate the distance between the discrete perovskite inorganic layers ranging from 18.6 to 27.1 Å, depending on the size of the fluorous cations (see SI Table S1). On the other side, XRD measurements on single crystals reveal that single inorganic layers of PbI_6 with <001>-terminated corner-sharing octahedra are spaced by the organic barrier, forming an alternating organic−inorganic layered structure as shown in Figure 1b. Notably, we derived the spacing between the inorganic planes which matches very well with the data obtained from thin film XRD (see SI Table S1). More in details, the XRD refinement procedure assigns the crystalline structures of the fluorous 2D HPs to the triclinic *P-1* space group (**$(A42)_2PbI_4$** and **$(A43)_2PbI_4$**) and monoclinic *C2c* space group (**$(A44)_2PbI_4$**). The corresponding cells parameters are listed in SI Table S2. The structures reported in Table 1 refer to an equivalent representation of the crystalline structure for the four compounds shown in SI Table S2. This new representation has been constructed in the framework of **$(A43)_2PbI_4$**, considered as a reference. More in details, in all cases, the cells consist of two chemical units and one inorganic layer. This approach enabled an easier comparison among the crystalline cells resulting from the different cations. It is fair noticing indeed that the derived interplane distances (among the inorganic layers) parallel the length of the organic cations following the same trend which increases from **A42** to **A44**. This, on the other side, reduced the computational workload, without compromising on the accuracy of the results. Because of the dynamic disorder typical of hybrid perovskites at room temperature, the present single crystal measurements lack of information on the position of the organic cations. Hence, reasonable guess for the conformation and position of the organic cations within the cells have been obtained from *ab initio molecular dynamics* simulations, as described in the SI. The obtained crystalline structures (inorganic structure and lattice parameters from XRD measurements and organic structure from simulations) are depicted in Figure 2 and SI Figure S3. To evaluate the optical properties of the 2D HPs, we have first measured the UV−vis absorption spectrum and

DOI: 10.1021/acs.chemmater.8b03377
Chem. Mater. 2018, 30, 8211−8220

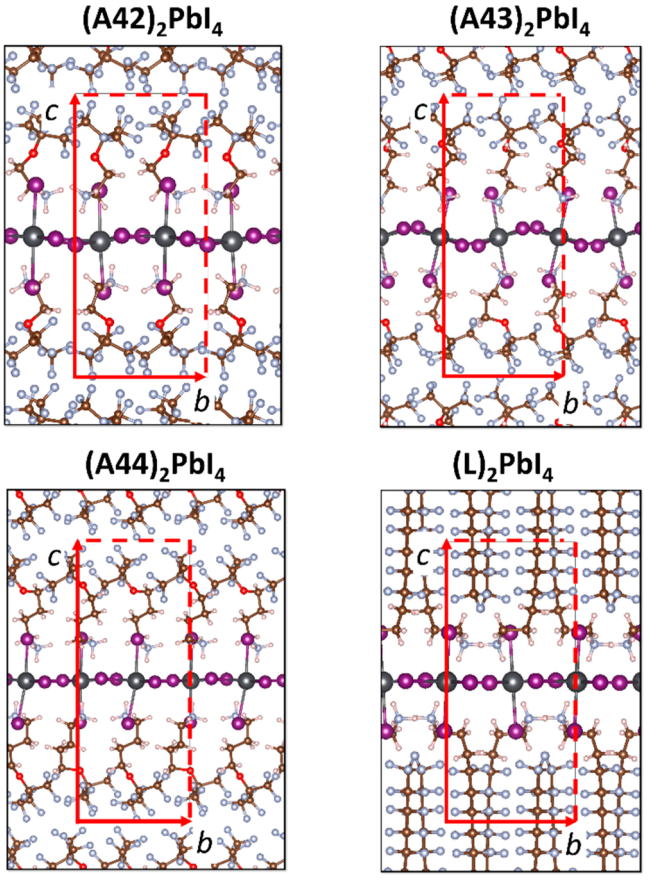

Figure 2. DFT simulations of the corresponding 2D HP structures. The crystalline cell is highlighted in red; the color scale is lead: black; iodine: violet; carbon: brown; oxygen: red; nitrogen: pale blue; fluorine: silver.

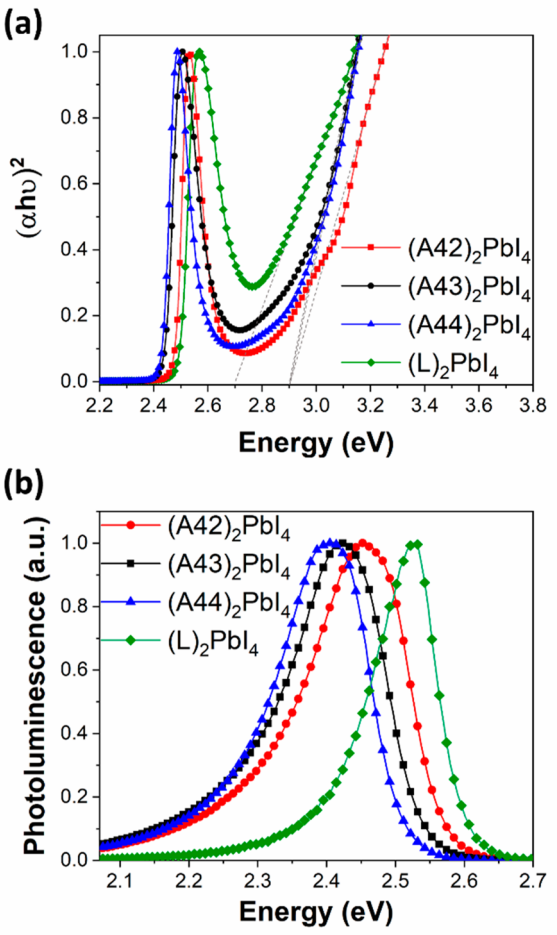

Figure 3. (a) UV−vis absorption spectrum of the four investigated 2D HPs. The plot reports also the electronic band gap, as extrapolated from Tauc linear fit (gray dashed lines). (b) Normalized PL spectra ($\lambda_{excitation}$ = 367 nm) of **(A42)$_2$PbI$_4$**, **(A43)$_2$PbI$_4$**, **(A44)$_2$PbI$_4$**, and **(L)$_2$PbI$_4$** in thin films at room temperature.

Table 2. Exciton Binding Energy (Eb) and Band Gap of (A42)$_2$PbI$_4$, (A43)$_2$PbI$_4$, (A44)$_2$PbI$_4$, and (L)$_2$PbI$_4$ Derived from the Tauc-Plot of Figure 3 Compared to the Band Gap Derived from DFT Calculations

	(A42)$_2$PbI$_4$	(A43)$_2$PbI$_4$	(A44)$_2$PbI$_4$	(L)$_2$PbI$_4$
Eb (meV)	380	393	420	130
band gap Tauc. (eV)	2.9	2.9	2.9	2.7
band gap DFT (eV)	3.0	3.1	3.0	2.8

estimated the material band gap through a Tauc plot analysis (see Figure 3a). For all the investigated systems, absorption spectra reveal a sharp and intense peak at around ∼2.5−2.6 eV, assigned to the excitonic feature, as typical for 2D HPs,[29,45,46] followed by a continuum absorption signal, related to direct band-to-band transitions. In the case of the branched systems, the band gap is 2.9 eV, almost independent from the structure of the cation, whereas the exciton binding energy (around 400 meV) experiences only a very small increase going from the shorter **A42** cation to the longer **A43** and **A44**, see Table 2.

Conversely, the absorption of the **(L)$_2$PbI$_4$** compound shows a blue-shifted excitonic peak along with a red-shifted band edge, with respect to the branched one, giving an estimation of the band gap of 2.7 eV. Notably, in this case, the exciton binding energy reduces to around 130 meV. To complete the investigation on the electronic properties of these compounds, we performed periodic DFT calculations, within the planewave/pseudopotential approach, as implemented in the Quantum-Espresso suite.[47] Contrary to the case of their parental 3D compounds, standard GGA calculations do not provide accurate results for 2D perovskites, compared to the experiments (see SI Figure S9).[28,48,49] This, because relativistic spin−orbit coupling[50] and electronic exchange-correlation affect the perovskite band gap to a different extent, and they do not cancel out each other, as in the case of methylammonium lead iodide perovskite.[51,52] To overcome this limitation, we performed here DFT simulations with hybrid DFT exchange-correlation functional (PBE0 with 30% of Hartree−Fock exchange) and including spin−orbit coupling. We verified in a previous work that the present approach is able to provide accurate band gap for the case of alkylammonium lead iodide perovskites.[28] The theoretical band gaps values computed from DFT agree very well with the experimental data for all the compounds (2.98, 2.96, and 2.81 eV for **A42**, **A44**, and **L**, respectively) except for the **A43** cation, where an overestimated band gap of 3.12 eV has been predicted (see Table 2).

Importantly, the DFT calculations are able to reproduce the ∼0.2 eV shift of the band gap from the linear compound to the branched compound. Figure 3b shows the photoluminescence (PL) spectra for the different compounds. First, it is worth pointing out that the materials derived from the branched

DOI: 10.1021/acs.chemmater.8b03377
Chem. Mater. 2018, 30, 8211−8220

family of cations (**A42**, **A43**, and **A44**) show a main emission peak that experiences a red shift with increasing cation length, matching the shift of the excitonic peak in absorption, whereas a blue-shifted emission is consistently observed for the **L**-based material (see SI Table S4). This enables us to conclude that the emission is excitonic in nature, due to the high oscillator strength of the quantum confined exciton as already observed for different 2D HP systems.[53,54] The PL decays at peak position are displayed in SI Figure S4 and Table S3. The decay can be fitted with a two-exponential function giving a fast time constant of τ_1 = 15 ns for the branched cations (**A42**, **A43**, **A44**) and τ_1 = 6.9 ns for the linear one-based 2D HPs and a longer-living tail. The fast decay, which dominates in amplitude, can be associated with excitonic recombination, in line with literature reports,[55,56] whereas the tail can be related to trap-mediated recombination. From a closer inspection of the PL spectra, we notice that the bandwidth of the PL spectra is different between the branched and the linear cations (SI Figure S5), much sharper for the last. It exhibits a Lorentz shape with a bandwidth (fwhm) of 0.11 eV, signature of purely excitonic emission. For the branched cations, a broader emission of width ∼0.15−0.17 eV is observed, with a tail extended more to the red. A simple two-Gaussian fit of the inhomogeneous broadening of the PL spectrum reveals the presence of a second emission peak at room temperature, red-shifted with respect to the main exciton peak. The origin of this secondary signal can be potentially related to the contribution of trap-assisted recombination from excitons trapped in defects, generated from strong exciton-lattice coupling, common in metal halides.[57] To further corroborate the observed trend, we also examined the absorption and emission properties of materials obtained using the branched cation **A43** and the linear one **L** mixed with lead bromide instead of lead iodide as inorganic component, resulting in the formation of an R_2PbBr_4 structure. The substitution of iodine with bromine results in a widening of the band gap manifested as a blue shift of the absorption spectrum, as known for Br-based perovskites.[24,58,59] Even in the case of $(\mathbf{L})_2\mathbf{PbBr}_4$ we could observe a sharper excitonic emission with bandwidth of 0.29 eV, compare to 0.39 eV for $(\mathbf{A43})_2\mathbf{PbBr}_4$ (see SI Figure S6).

Theoretical Calculations of 2D HPs: Band Gap, Dielectric Properties, Electronic Structure, and Charge Carrier Effective Masses. In light of the capability of DFT to reproduce the red shift of the band gap when going from the branched compounds to the linear one, we tried to rationalize this striking result that originates from the nature of the organic, saturated cation. As previously mentioned above, two mechanisms have been reported in the literature to explain the dependence of the electronic properties of 2D HPs on the organic cation. The first is via direct influence on the electronic structure of the inorganic frame, due to the dielectric properties of the organic cation.[24,25] The second is via indirect influence, induced by the structural distortion of the inorganic sheet.[27,28] In Figure 4a, we show the inorganic structure of $(\mathbf{A42})_2\mathbf{PbI}_4$, taken as reference for the branched compounds, and of $(\mathbf{L})_2\mathbf{PbI}_4$ compound, together with the values of the Pb−I−Pb angles. The $(\mathbf{L})_2\mathbf{PbI}_4$ compound is characterized by larger Pb−I−Pb angle, compared to the $(\mathbf{A42})_2\mathbf{PbI}_4$, a feature which has been already associated with more dispersed valence and conduction bands and, consequently, to a smaller band gap.[25,28] This fact hence already suggests the predominant role of the structural distortions in band gap tuning as reported in

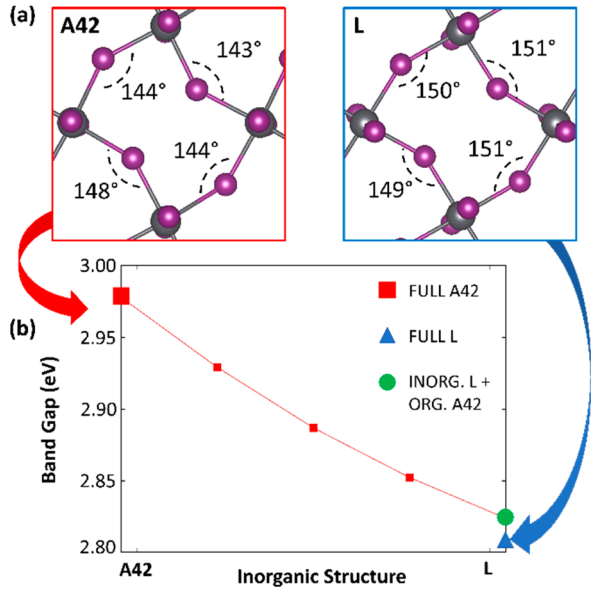

Figure 4. (a) Inorganic structure and Pb−I−Pb bond angles of the $(\mathbf{A42})_2\mathbf{PbI}_4$ and $(\mathbf{L})_2\mathbf{PbI}_4$ perovskites; (b) Variation of the band gap of 2D HPs models, with inorganic frame varying from the $(\mathbf{A42})_2\mathbf{PbI}_4$ to the $(\mathbf{L})_2\mathbf{PbI}_4$. The band gap of the $(\mathbf{A42})_2\mathbf{PbI}_4$ (red square) and $(\mathbf{L})_2\mathbf{PbI}_4$ (blue triangle) is also reported, together with the band gap of the mixed systems, with inorganic frame from **L** and organic **A42** cations.

Figure 3a. To definitely disentangle the relative importance of dielectric screening and structural distortions on the bandgap, we devised the following computational experiment. Considering the $(\mathbf{L})_2\mathbf{PbI}_4$ and the $(\mathbf{A42})_2\mathbf{PbI}_4$ systems, we took the inorganic structure of the former and introduced the organic cation from the latter. Hence, in the case of pure indirect structural effect, the bang gap of the mixed model should be the same of that of the full $(\mathbf{L})_2\mathbf{PbI}_4$ structure. At the opposite, in the case of a main direct effect of the organic cation on the electronic structure of the perovskite, the band gap of the mixed model should resemble that of the full $(\mathbf{A42})_2\mathbf{PbI}_4$ system, in spite of the structural differences showed in Figure 4a. The band gap, computed as a function of the considered inorganic structure, is reported in Figure 4b. Results clearly show that the mixed model (inorganic from $(\mathbf{L})_2\mathbf{PbI}_4$ and organic from $(\mathbf{A42})_2\mathbf{PbI}_4$) has a band gap very similar to that of the full $(\mathbf{L})_2\mathbf{PbI}_4$ compound. To further strengthen this result, we have computed the band gap for three intermediate 2D HPs models containing the **A42** cation but having an inorganic structure which is intermediate between the one from $(\mathbf{A42})_2\mathbf{PbI}_4$ and the one from $(\mathbf{L})_2\mathbf{PbI}_4$. The monotonic dependence of the band gap from the inorganic structure definitely demonstrates its dominant role for the systems under investigation. Figure 4b also indicates that the role of the organic spacers in affecting the electronic properties of these systems is limited to only of few meV. Another important aspect is the variation of the exciton binding energy observed when branched (**A4n**) versus linear (**L**) cations are used (see Figure 3a and Table 2). To address this, we performed time-dependent (TD) DFT calculations, a formalism which allows simulation of the formation of exciton, via the collective response of the electrons in the system, conceptually associated with the dynamic dielectric constant (ε_∞).[60] Our TDDFT simulations in SI Figure S10 provided similar exciton binding energies, around 550 meV, in the range of the experimental

DOI: 10.1021/acs.chemmater.8b03377
Chem. Mater. 2018, 30, 8211−8220

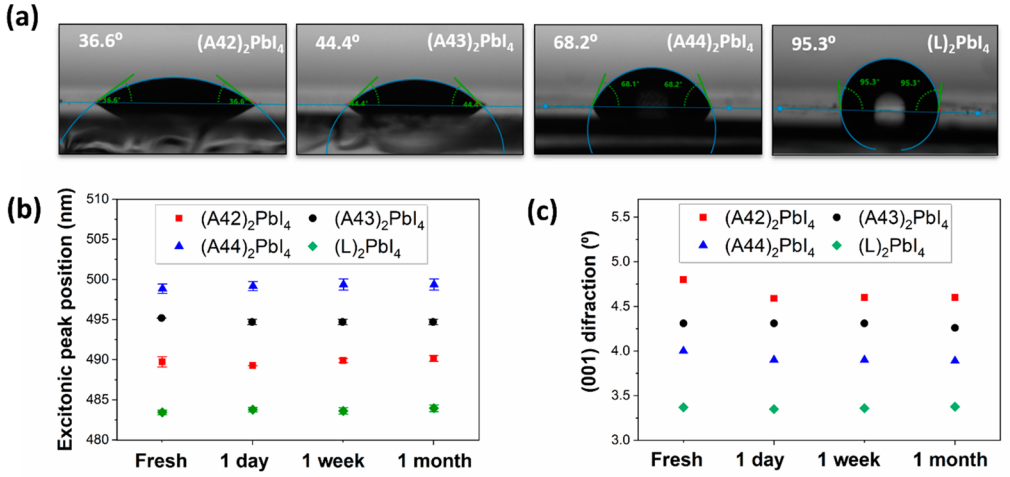

Figure 5. (a) Illustration of the contact angle formed by a water drop on $(\mathbf{A42})_2\mathbf{PbI}_4$, $(\mathbf{A43})_2\mathbf{PbI}_4$, $(\mathbf{A44})_2\mathbf{PbI}_4$ and $(\mathbf{L})_2\mathbf{PbI}_4$ in thin films (36.6°, 44.4° 68.2°, 95.3° respectively); Stability study of the 2D HPs in thin film stored in air: (b) Position of the maximum absorption peak, (c) Position of (001) X-ray diffraction, after the preparation, after 1 day, 1 week and one month.

values obtained for the materials investigated (see SI Table S4). Trying to better understand the difference in the excited state properties of these compounds, we further computed the dynamic dielectric constant (ε_∞) of the **A42** and **L** based 2D material, which dictates the screening of the photogenerated electron−hole induced by the electron density. This was calculated along the three Cartesian axes, by using DFT simulations in the presence of an external electric field.[61] In line with the results from TDDFT, we found very similar dielectric constant for the **A42** (2.22, 2.18, and 1.63 along the *x*, *y*, and *z* direction, respectively, with the latter corresponding to the direction of the inorganic stacking) and for the **L** compound (2.26, 2.30, and 1.76 along *x*, *y*, and *z*, respectively). Hence, the strikingly different exciton binding energy found in Figure 3a for branched and linear compound cannot be explained on the basis of different screening by the electronic mean-field density, as estimated by the dynamic dielectric constant (ε_∞). On the other hand, a recent theoretical investigation on the parental 3D metal halide perovskites suggested the importance of low energy phonons in determining the exciton binding energy. Namely, the correct value of the exciton binding energy for the prototypical $CH_3NH_3PbI_3$ perovskite is computed, when an effective dielectric constant of 15 is considered, which lies in the middle between the static (ε_0) and the dynamic (ε_∞) dielectric constant reported for this material.[62] From this value, we can retrieve an esteem of the exciton binding energy (considering $E_b = \frac{m^* e^4}{\hbar^2 \varepsilon^2}$) of around 400 meV, in line with what found. Finally, we have calculated the band structure, partial density of states and effective masses of the charge carriers. In SI Figure S11, we report the band structure of the four 2D HPs, as calculated adopting PBE exchange-correlation functional and including spin−orbit coupling. The partial density of states reveals that the valence band is mainly constituted by atomic orbitals from the iodine atoms, whereas the conduction band is due to similar contributions from lead and iodide. As in the case of alkylammonium 2D lead iodide perovskites, organic atoms contribute to crystalline orbitals only 0.5 eV below the valence band edge and several eV above the conduction band edge, hence being not involved in the optoelectronic processes. The band gap is expectedly underestimated, due to the lack of an accurate treatment of the electron exchange-correlation. Conversely, a more refined treatment of the exchange interaction energy for the calculation of the band dispersion is prohibitively expensive for the present systems. Interestingly, the valence and conduction band edges are found in proximity of the center of the first Brillouin zone (Γ). A Rashba-Dresselhaus splitting, which consists of the splitting of the two angular components of the electronic bands in the reciprocal space, is observed. This type of feature has been widely investigated in the case of hybrid perovskites in general, and it is associated with the concomitant presence of spin−orbit coupling together with an internal electric field in the material.[63,64] The effective masses of free charge carriers are listed in SI Table S7, for the four 2D HPs investigated.

Charge carriers have effective masses of a few tenths the electron mass within the inorganic plane, while they are much larger along the direction of the inorganic-sheet stacking, as expected because of the presence of the organic spacers. The effective masses in SI Table S7 are somewhat larger than those computed for the polymorphs of the 2D hexylammonium and docecylammonium lead iodide HP.[28] Nevertheless, these effective masses are still small, especially compared to those estimated for the best organic semiconductors.[65,66] As in the case for the band gap, the $(\mathbf{L})_2\mathbf{PbI}_4$ compound is characterized by smaller effective masses, compared to the $(\mathbf{A4n})_2\mathbf{PbI}_4$ materials and it is hence expected to show improved transport properties.

2D HPs Stability Tests. As stated in the introduction, we designed the new family of fluorous 2D HP with the final aim to increase the water-repellent character of the ultimate perovskite thin film. To verify the robustness upon water exposure and the hydrophobic character of the 2D HP, we carried out contact angle measurements using water. The results are displayed in Figure 5a. On one hand, the 2D HPs based on **L** cation exhibits a clear hydrophobic character, in line with the typical behavior of materials with highly ordered linear perfluoroalkyl chains at the outermost surface.[67] On the other hand, for materials based on **A4n** salts, the contact angle increases with the length of the alkylene linker present in the branched organic cations (from **A42** to **A44**), but remains <90°. This is not totally unexpected, because of the higher

DOI: 10.1021/acs.chemmater.8b03377
Chem. Mater. 2018, 30, 8211−8220

mobility of the branched fluorinated segment with respect to the linear one, which provides frustrated packing and a reduced water shielding effect.[68] Then, to test the long-term stability, we evaluated the variation of the optical and structural properties of the 2D HPs thin films upon exposing the samples in air (relative humidity = 40%) for more than one month. Figure 5b,c shows the data collected by monitoring the R_2PbI_4 maxima absorption position and (001) diffraction position at different time exposure. As seen in Figure 5b, the excitonic peak remains at the same position over time for all 2D HPs investigated. In addition, no distinct differences were observed in the position of the (001) diffraction peak of the 2D HPs stored in air, after the different times of exposure (Figure 5c). This provides compelling evidence of the high degree of stability and resistance of the fluorous perovskite films in ambient conditions.

CONCLUSIONS

In this work, we have synthesized a new series of fluorous organic cations and shaped them to form tunable and stable 2D HPs. The fluorous cations impart extreme stability of the 2D HPs upon exposure to atmosphere conditions and enhance the water-repellent character of the 2D HP surface. Shorter-branched and longer-linear fluorous cations have been designed as the organic barriers for the fluorous 2D HPs. The size and shape of the organic cation modulate the 2D HP structure, electronic, and optical properties. Despite the fact that the organic spacers do not participate in the electronic structure, they influence the perovskites electronic structure via an indirect structural effect on the inorganic sheet, inducing a variation of the band gap and exciton binding energy. These local distortions affect the binding energy more than local dielectric mismatch. The longer the cation, the smaller the band gap. This results in a lower exciton binding energy and smaller effective masses, pointing toward a better transport for the elongated fluorous chains. This new family of stable 2D HPs not only shows the large extent of tuning the optoelectronic properties by simple shaping of the fluorous organic spacer, but, importantly, it shows a remarkably high structural stability kept intact even upon a one-month air exposure. Overall, these attributes make this fluorous 2D HP an exciting candidate for stable perovskite optoelectronics.

EXPERIMENTAL SECTION

Materials and Methods. All available chemicals and solvents were purchased from commercial sources and were used without any further purification. (*N*-hydroxyalkyl)amino phthalimides **1a**–**c**,[69,70] *N*-allyl phthalimide **3**,[71] and 2-(4,4,5,5,6,6,7,7,8,8,9,9,9-tridecafluoro-2-iodo-nonyl)-isoindole-1,3-dione **4**[72] were prepared as described in the literature. Reactions were monitored by thin layer chromatography (TLC) that was conducted on plates precoated with silica gel Si 60-F254 (Merck, Germany). Column chromatography was conducted by using silica gel Si 60, 230–400 mesh, 0.040–0.063 mm (Merck, Darmstadt, Germany). ^{1}H and ^{13}C NMR spectra were recorded on a Bruker Avance 400 (400 and 100.6 MHz, respectively); chemical shifts are indicated in parts per million downfield from $SiMe_4$, using the residual proton ($CHCl_3$ = 7.26 ppm, CHD_2SOCD_3 = 2.50 ppm, CHD_2OD = 3.33 ppm) and carbon ($CDCl_3$ = 77.0 ppm, $(CD_3)_2SO$ = 40.45 ppm, CD_3OD = 49.10 ppm) solvent resonances as the internal reference. ^{19}F NMR spectra were recorded on a Bruker AC 300 spectrometer (282 MHz) and a Bruker Avance 400 (377 MHz). Coupling constant values J are given in Hz. Elemental analyses were carried out by the Departmental Service of Microanalysis (at University of Milano).

General Procedure for the Mitsunobu Reaction. In a flame-dried Schlenk tube equipped with a magnetic stirrer (*N*-hydroxyalkyl)amino phthalimide **1** (10 mmol) and PPh_3 (12 mmol) were suspended in dry Et_2O (50 mL) under nitrogen. After cooling at 0 °C, perfluoro-*tert*-butanol (10 mmol) was added followed by the dropwise addition of a solution of diisopropyl azodicarboxylate (DIAD, 12 mmol) in dry Et_2O (8 mL) in 5 min. The mixture was left to attain room temperature and then stirred overnight. The mixture was filtered, the solvent was removed at reduced pressure, and the residue purified by column chromatography.

*2-[2-(Nonafluoro-tert-butyloxy)-ethyl]isoindole-1,3-dione (**2a**).* This product was obtained using the standard Mitsunobu procedure starting from **1a**(1.91 g, 10 mmol) and perfluoro-*tert*-butanol (1.4 mL, 10 mmol). Crude material was purified by column chromatography (silica gel, petroleum ether/diethyl ether 4/1) to give the title compound (3.26 g, 79.6% yield) as a white solid. ^{1}H NMR (400 MHz, $CDCl_3$) δ = 7.88 (dd, ^3J = 5.4, 3.1, 2H), 7.74 (dd, ^3J = 5.5, 3.1, 2H), 4.27 (t, ^3J = 5.5, 2H), 4.01 (t, ^3J = 5.5, 2H). ^{13}C NMR (100.6 MHz, $CDCl_3$) δ 167.8, 134.2, 131.8, 123.4, 120.1 (q, $^1J_{CF}$ = 293.9), 79.8 (m), 66.6, 37.4. ^{19}F NMR (282 MHz, $CDCl_3$) δ = −71.01 (s). Anal. Calcd for $C_{14}H_8F_9NO_3$: C 41.09, H 1.97, N 3.42. Found: C 41.05, H 1.96, N 3.40.

*2-[3-(Nonafluoro-tert-butyloxy)-propyl]isoindole-1,3-dione (**2b**).* This product was obtained using the standard Mitsunobu procedure starting from **1b**(2.05 g, 10 mmol) and perfluoro-*tert*-butanol (1.4 mL, 10 mmol). Crude material was purified by chromatography (silica gel, petroleum ether/diethyl ether 4/1) to give the title compound (3.50 g 82.8% yield) as a white solid. ^{1}H NMR (400 MHz, $CDCl_3$) δ = 7.84 (dd, ^3J = 5.4, 3.0, 2H), 7.71 (dd, ^3J = 5.5, 3.0, 2H), 4.11 (t, ^3J = 6.0, 2H), 3.81 (t, ^3J = 7.0, 2H), 2.10 (quintet, ^3J = 6.4, 2H). ^{13}C NMR (100.6 MHz, $CDCl_3$) δ 168.3, 134.1, 132.2, 123.4, 120.3 (q, $^1J_{CF}$ = 290.7), 79.7 (m), 67.8, 34.9, 28.9. ^{19}F NMR (282 MHz, $CDCl_3$) δ = −70.82 (s). Anal. Calcd for $C_{15}H_{10}F_9NO_3$: C 42.57, H 2.38, N 3.31. Found: C 42.53, H 2.39, N 3.30.

*2-[4-(Nonafluoro-tert-butyloxy)-butyl]isoindole-1,3-dione (**2c**).* This product was obtained using the standard Mitsunobu procedure starting from **1c**(2.19 g, 10 mmol) and perfluoro-*tert*-butanol (1.4 mL, 10 mmol). Crude material was purified by chromatography (silica gel, petroleum ether/diethyl ether 4/1) to give the title compound (3.58 g, 81.9% yield) as a white solid. ^{1}H NMR (400 MHz, $CDCl_3$) δ = 7.84 (dd, ^3J = 5.4, 3.0, 2H), 7.71 (dd, ^3J = 5.4, 3.1, 2H), 4.04 (t, ^3J = 5.8, 2H), 3.72 (t, ^3J = 6.8, 2H), 1.90–1.61 (m, 4H). ^{13}C NMR (100.6 MHz, $CDCl_3$) δ 168.5, 134.1, 132.2, 123.4, 120.5 (q, $^1J_{CF}$ = 291.8), 80.0 (m), 69.2, 37.4, 27.2, 24.8. ^{19}F NMR (377 MHz, $CDCl_3$) δ = −71.35 (s). Anal. Calcd for $C_{16}H_{12}F_9NO_3$: C 43.95, H 2.77, N 3.20. Found: C 43.88, H 2.76, N 3.22.

*2-(4,4,5,5,6,6,7,7,8,8,9,9,9-Tridecafluorononyl)isoindole-1,3-dione (**5**).* To a solution of iodide **4** (4 g, 6.32 mmol) and Et_3N (1 mL, 7.17 mmol) in dry THF (7 mL) in a stainless steel reactor, 10% Pd/C (125 mg) was added. The reactor was pressurized with H_2 (4 atm) at room temperature. After 24 h, the pressure was released and the mixture was filtered through a short pad of Celite and concentrated under vacuum. The residue was purified by chromatography (silica gel, petroleum ether/methylene chloride 7/3) affording the title compound (2.89 g, 90.4% yield) as a white solid. ^{1}H NMR (400 MHz, $CDCl_3$) δ = 7.86 (dd, ^3J = 5.4, 3.0, 2H), 7.73 (dd, ^3J = 5.4, 3.1, 2H), 3.78 (t, ^3J = 6.9, 2H), 2.29–2.07 (m, 2H), 2.07–1.93 (m, 2H). ^{13}C NMR (100.6 MHz, $CDCl_3$) δ 168.3, 134.3, 132.1, 123.5, 121–105 (m, C_6F_{13}), 37.2, 28.8 (t, $^1J_{CF}$ = 22.7), 20.1. ^{19}F NMR (377 MHz, $CDCl_3$) δ = −81.77 (t, ^3J = 10.1, 3F), −115.24 (m, 2F), −122.94 (m, 2F), −123.89 (m, 2F), −124.38 (m, 2F), −127.14 (m, 2F). Anal. Calcd for $C_{17}H_{10}F_{13}NO_2$: C 40.25, H 1.99, N 2.76. Found: C 40.38, H 1.98, N 2.74.

General Procedure for the Hydrazinolysis of Phthalimide Derivatives. To a solution of phthalimide derivative (1 mmol) in MeOH (2 mL), hydrazine monohydrate (1.2 mmol, 60 μL) was added and the solution refluxed for 3 h. After cooling, the mixture was filtered through a Büchner funnel to remove the solid phthalhydrazide. The clear methanolic solution was treated with 50% aqueous HI (0.18 mL, 1.2 mmol). The solution was stirred overnight at room

DOI: 10.1021/acs.chemmater.8b03377
Chem. Mater. 2018, 30, 8211–8220

temperature. The solvent was removed at reduced pressure and the residue was dissolved in the minimal amount of MeOH and precipitated from diethyl ether. After filtration, the solid material was dried under vacuum.

*2-(Nonafluoro-tert-butyloxy)ethylamine hydroiodide (**A42**).* Hydrazinolysis of **2a**(3.00 g, 7.33 mmol) afforded the title compound (2.34 g, 78.4% yield) as a white solid. ^{1}H NMR (400 MHz, DMSO) δ = 7.82 (s, 3H), 4.27 (t, ^{3}J = 5.2, 2H), 3.17 (t, ^{3}J = 5.2, 2H). ^{13}C NMR (100.6 MHz, DMSO) δ = 119.8 (q, $^{1}J_{CF}$ = 293.3), 79.2 (m), 67.0, 38.6. ^{19}F NMR (282 MHz, $CDCl_3$) δ = −70.97 (s).

*3-(Nonafluoro-tert-butyloxy)propylamine hydroiodide (**A43**).* Hydrazinolysis of **2b**(3.00 g, 7.08 mmol) afforded the title compound (2.28 g, 76.5% yield) as a white solid. ^{1}H NMR (400 MHz, DMSO) δ = 7.56 (s, 3H), 4.18 (t, ^{3}J = 6.2, 2H), 2.96−2.80 (m, 2H), 2.06−1.80 (m, 2H). ^{13}C NMR (100.6 MHz, DMSO) δ = 119.9 (q, $^{1}J_{CF}$ = 291.8), 79.36 (m), 67.78, 35.53, 27.49. ^{19}F NMR (282 MHz, $CDCl_3$) δ = −70.97 (s).

*4-(Nonafluoro-tert-butyloxy)butylamine hydroiodide (**A44**).* Hydrazinolysis of **3c**(2.04 g, 4.67 mmol) afforded the title compound (1.33 g, 65.5% yield) as a white solid. ^{1}H NMR (400 MHz, MeOD) δ = 4.15 (d, ^{3}J = 5.3, 2H), 3.10−2.86 (m, 2H), 1.83−1.72 (m, 4H). ^{13}C NMR (100.6 MHz, MeOD) δ 120.4 (q, $^{1}J_{CF}$ = 292.9), 81.0 (m), 70.9, 40.4, 27.84, 25.06. ^{19}F NMR (377 MHz, $CDCl_3$) δ = −72.70 (s).

*4,4,5,5,6,6,7,7,8,8,9,9,9-Tridecafluorononylamine hydroiodide (**L**).* Hydrazinolysis of **5**(1.00 g, 1.97 mmol) afforded the title compound (0.75 g, 65.5% yield) as a white solid. ^{1}H NMR (400 MHz, DMSO) δ = 7.71 (s, 3H), 2.94 (s br, 2H), 2.39 (m, 2H), 1.81 (m, 2H). ^{13}C NMR (100.6 MHz, DMSO) δ 121−107 (m, C_6F_{13}), 37.9, 26.9 (t, $^{1}J_{CF}$ = 21.2), 18.3. ^{19}F NMR (377 MHz, DMSO) δ = −81.22 (t, ^{3}J = 10.0, 3F), −114.56 (m, 2F), −122.73 (m, 2F), −123.67 (m, 2F), −124.19 (m, 2F), −126.78 (m, 2F).

■ ASSOCIATED CONTENT

Supporting Information

The Supporting Information is available free of charge on the ACS Publications website at DOI: 10.1021/acs.chemmater.8b03377.

Additional data (in terms of scanning electron microscopy imagines, crystallographic data and details of the structure refinement, PL decay, computational details, and RMN spectra), and experimental details (PDF)

■ AUTHOR INFORMATION

Corresponding Author

*E-mail: giulia.grancini@epfl.ch.

ORCID

Claudio Quarti: 0000-0002-5488-1216
Simonetta Orlandi: 0000-0001-6783-4243
Andreas Lesch: 0000-0002-4995-2251
David Beljonne: 0000-0002-2989-3557
Mohammad Khaja Nazeeruddin: 0000-0001-5955-4786
Giulia Grancini: 0000-0001-8704-4222

Author Contributions

I.G.-B planned the experiments, developed the 2D HPs and characterized them; V I.E.Q. performed the PL measurements, I.Z. developed and characterized the single crystals; C.Q. and D.B. carried out the theoretical analysis and contributed in the discussion. S.O., M.C., and G.P. synthesized the new compounds and planned the work; A.L. assisted in the contact angle measurements. S.M. assisted in the XRD measurements and analysis. G.P., M.K.N., and G.G. conceived the idea. G.G. supervised the research project. All the authors contribute in writing or revising the paper.

Funding

Swiss National Science Foundation (SNSF) funding through the Ambizione Energy project HYPER (Grant Number PZENP2173641).

Notes

The authors declare no competing financial interest.

■ ACKNOWLEDGMENTS

We acknowledge the Swiss National Science Foundation (SNSF) funding through the Ambizione Energy project HYPER (Grant Number PZENP2173641). The DFT simulations activity was supported by the Fonds de la Recherche Scientifique de Belgique (F.R.S.-FNRS). Computational resources have been provided by the Consortium des Équipements de Calcul Intensif (CÉCI). D.B. is a FNRS Research Director. We acknowledge Prof. Raffaella Buonsanti for the use of the Fluorolog system for the data reported in SI Figure S3 and Cristina Roldán Carmona for the SEM images shown in SI Figure S1. We thank Dr. Mirko Prato for useful discussion. S.O., M.C., and G.P. thank the CNR/Regione Lombardia project "Integrated Zero Emission Buildings". We acknowledge the Toyota Technical Centre through the project PeLED.

■ REFERENCES

(1) Snaith, H. J. Present status and future prospects of perovskite photovoltaics. *Nat. Mater.* **2018**, *17*, 372−376.

(2) Sun, J.; Wu, J.; Tong, X.; Lin, F.; Wang, Y.; Wang, Z. M. Organic/Inorganic Metal Halide Perovskite Optoelectronic Devices beyond Solar Cells. *Adv. Sci.* **2018**, *5*, 1700780−1700793.

(3) Ye, H.-Y.; Tang, Y.-Y.; Li, P.-F.; Liao, W.-Q.; Gao, J.-X.; Hua, X.-N.; Cai, H.; Shi, P.-P.; You, Y.-M.; Xiong, R.-G. Metal-free three-dimensional perovskite ferroelectrics. *Science* **2018**, *361*, 151−155.

(4) Liao, W.-Q.; Zhang, Y.; Hu, C.-L.; Mao, J.-G.; Ye, H.-Y.; Li, P.-F.; Huang, S. D.; Xiong, R.-G. A lead-halide perovskite molecular ferroelectric semiconductor. *Nat. Commun.* **2015**, *6*, 1−7.

(5) Jeon, N. J.; Na, H.; Jung, E. H.; Yang, T.-Y.; Lee, Y. G.; Kim, G.; Shin, H.-W.; Seok, S. I.; Lee, J.; Seo, J. A fluorene-terminated hole-transporting material for highly efficient and stable perovskite solar cells. *Nat. Energy* **2018**, *3*, 682−689.

(6) Green, M. A.; Hishikawa, Y.; Dunlop, E. D.; Levi, D. H.; Hohl-Ebinger, J.; Ho-Baillie, A. W. Y. Solar cell efficiency tables (version 51). *Prog. Photovoltaics* **2018**, *26*, 3−12.

(7) Poorkazem, K.; Kelly, T. L. Compositional engineering to improve the stability of lead halide perovskites: A Comparative study of cationic and anionic dopants. *ACS Appl. Energy Mater.* **2018**, *1*, 181−190.

(8) Zhang, X.; Ren, X.; Liu, B.; Munir, R.; Zhu, X.; Yang, D.; Li, J.; Liu, Y.; Smilgies, D.-M.; Li, R.; Yang, Z.; Niu, T.; Wang, X.; Amassian, A.; Zhao, K.; Liu, S. F. Stable high efficiency two-dimensional perovskite solar cells via cesium doping. *Energy Environ. Sci.* **2017**, *10*, 2095−2102.

(9) Fu, Q.; Tang, X.; Huang, B.; Hu, T.; Tan, L.; Chen, L.; Chen, Y. Recent Progress on the Long-Term Stability of Perovskite Solar Cells. *Adv. Sci.* **2018**, *5*, 1700387−1700404.

(10) Grancini, G.; Roldán-Carmona, C.; Zimmermann, I.; Mosconi, E.; Lee, X.; Martineau, D.; Narbey, S.; Oswald, F.; De Angelis, F.; Graetzel, M.; Nazeeruddin, M. K. One-Year stable perovskite solar cells by 2D/3D interface engineering. *Nat. Commun.* **2017**, *8*, 15684−15692.

(11) Stoumpos, C. C.; Cao, D. H.; Clark, D. J.; Young, J.; Rondinelli, J. M.; Jang, J. I.; Hupp, J. T.; Kanatzidis, M. G. Ruddlesden−Popper Hybrid Lead Iodide Perovskite 2D Homologous Semiconductors. *Chem. Mater.* **2016**, *28*, 2852−2867.

DOI: 10.1021/acs.chemmater.8b03377
Chem. Mater. 2018, 30, 8211−8220

(12) Kieslich, G.; Sun, S.; Cheetham, A. K. An extended Tolerance Factor approach for organic−inorganic perovskites. *Chem. Sci.* **2015**, *6*, 3430−3433.
(13) Cao, D. H.; Stoumpos, C. C.; Farha, O. K.; Hupp, J. T.; Kanatzidis, M. G. 2D Homologous Perovskites as Light-Absorbing Materials for Solar Cell Applications. *J. Am. Chem. Soc.* **2015**, *137*, 7843−7850.
(14) Hong, X.; Ishihara, T.; Nurmikko, A. V. Dielectric Confinement Effect on Excitons in PbI_4-Based Layered Semiconductors. *Phys. Rev. B: Condens. Matter Mater. Phys.* **1992**, *45*, 6961−6964.
(15) Chong, W. K.; Thirumal, K.; Giovanni, D.; Goh, T. W.; Liu, X.; Mathews, N.; Mhaisalkar, S. G.; Sum, T. C. Dominant factors limiting the optical gain in layered two-dimensional halide perovskite thin films. *Phys. Chem. Chem. Phys.* **2016**, *18*, 14701−14708.
(16) Yangui, A.; Garrot, D.; Lauret, J. S.; Lusson, A.; Bouchez, G.; Deleporte, E.; Pillet, S.; Bendeif, E. E.; Castro, M.; Triki, S.; Abid, Y.; Boukheddaden, K. Optical Investigation of Broadband White-Light Emission in Self-Assembled Organic−Inorganic Perovskite $(C_6H_{11}NH_3)_2PbBr_4$. *J. Phys. Chem. C* **2015**, *119*, 23638−23647.
(17) Koutselas, I. B.; Ducasse, L.; Papavassiliou, G. C. Electronic properties of three- and low-dimensional semiconducting materials with Pb halide and Sn halide units. *J. Phys.: Condens. Matter* **1996**, *8*, 1217−1227.
(18) Ishihara, T.; Takahashi, J.; Goto, T. Optical properties due to electronic transitions in two-dimensional semiconductors $(C_nH_{2n+1}NH_3)_2PbI_4$. *Phys. Rev. B: Condens. Matter Mater. Phys.* **1990**, *42*, 11099−11107.
(19) Gan, L.; Li, J.; Fang, Z.; He, H.; Ye, Z. Effects of Organic Cation Length on Exciton Recombination in Two-Dimensional Layered Lead Iodide Hybrid Perovskite Crystals. *J. Phys. Chem. Lett.* **2017**, *8*, 5177−5183.
(20) Era, M.; Morimoto, S.; Tsutsui, T.; Saito, S. Organic-inorganic heterostructure electroluminescent device using a layered perovskite semiconductor $(C_6H_5C_2H_4NH_3)_2PbI_4$. *Appl. Phys. Lett.* **1994**, *65*, 676−678.
(21) Mitzi, D. B.; Chondroudis, K.; Kagan, C. R. Design, Structure, and Optical Properties of Organic−Inorganic Perovskites Containing an Oligothiophene Chromophore. *Inorg. Chem.* **1999**, *38*, 6246−6256.
(22) Kondo, T.; Azuma, T.; Yuasa, T.; Ito, R. Biexciton lasing in the layered perovskite-type material $(C_6H_{13}NH_3)_2PbI_4$. *Solid State Commun.* **1998**, *105*, 253−255.
(23) Kondo, T.; Iwamoto, S.; Hayase, S.; Tanaka, K.; Ishi, J.; Mizuno, M.; Ema, K.; Ito, R. Resonant third-order optical nonlinearity in the layered perovskite-type material $(C_6H_{13}NH_3)_2PbI_4$. *Solid State Commun.* **1998**, *105*, 503−506.
(24) Du, K.; Tu, Q.; Zhang, X.; Han, Q.; Liu, J.; Zauscher, S.; Mitzi, D. B. Two-Dimensional Lead(II) Halide-Based Hybrid Perovskites Templated by Acene Alkylamines: Crystal Structures, Optical Properties, and Piezoelectricity. *Inorg. Chem.* **2017**, *56*, 9291−9302.
(25) Traore, B.; Pedesseau, L.; Assam, L.; Che, X.; Blancon, J.-C.; Tsai, H.; Nie, W.; Stoumpos, C. C.; Kanatzidis, M. G.; Tretiak, S.; Mohite, A. D.; Even, J.; Kepenekian, M.; Katan, C. Composite Nature of Layered Hybrid Perovskites: Assessment on Quantum and Dielectric Confinements and Band Alignment. *ACS Nano* **2018**, *12*, 3321−3332.
(26) Misra, R. K.; Cohen, B.-E.; Iagher, L.; Etgar, L. Low-Dimensional Organic-Inorganic Halide Perovskite: Structure, Properties, and Applications. *ChemSusChem* **2017**, *10*, 3712−3721.
(27) Knutson, J. L.; Martin, J. D.; Mitzi, D. B. Tuning the Band Gap in Hybrid Tin Iodide Perovskite Semiconductors Using Structural Templating. *Inorg. Chem.* **2005**, *44*, 4699−4705.
(28) Quarti, C.; Marchal, N.; Beljonne, D. Tuning the Optoelectronic Properties of Two-Dimensional Hybrid Perovskite Semiconductors with Alkyl Chain Spacers. *J. Phys. Chem. Lett.* **2018**, *9*, 3416−3424.
(29) Gladysz, J. A.; Curran, D. P. Fluorous chemistry: from biphasic catalysis to a parallel chemical universe and beyond. *Tetrahedron* **2002**, *58*, 3823−3825.
(30) *Handbook of Fluorous Chemistry*; Gladysz, J. A., Curran, D. P., Horváth, I. T.; Eds.; Wiley-VCH: Weinheim Germany, 2004.
(31) Mitzi, D. B.; Medeiros, D. R.; Malefant, P. L. Intercalated Organic−Inorganic Perovskites Stabilized by Fluoroaryl−Aryl Interactions. *Inorg. Chem.* **2002**, *41*, 2134−2145.
(32) Wei, Y.; Lauret, J. S.; Galmiche, L.; Audebert, P.; Deleporte, E. Strong exciton-photon coupling in microcavities containing new fluorophenethylamine based perovskite compounds. *Opt. Express* **2012**, *20*, 10399−10405.
(33) Wei, Y.; Audebert, P.; Galmiche, L.; Lauret, J.-S.; Deleporte, E. Synthesis, optical properties and photostability of novel fluorinated organic−inorganic hybrid $(R{-}NH_3)_2PbX_4$ semiconductors. *J. Phys. D: Appl. Phys.* **2013**, *46*, 135105−135114.
(34) Wei, Y.; Audebert, P.; Galmiche, L.; Lauret, J.-S.; Deleporte, E. Photostability of 2D Organic-Inorganic Hybrid Perovskites. *Materials* **2014**, *7*, 4789−4802.
(35) Lermer, C.; Birkhold, S. T.; Moudrakovski, I. L.; Mayer, P.; Schoop, L. M.; Schmidt-Mende, L.; Lotsch, B. V. Toward Fluorinated Spacers for MAPI-Derived Hybrid Perovskites: Synthesis, Characterization, and Phase Transitions of $(FC_2H_4NH_3)_2PbCl_4$. *Chem. Mater.* **2016**, *28*, 6560−6566.
(36) Shi, E.; Gao, Y.; Finkenauer, B. P.; Akriti; Coffey, A. H.; Letian Dou, L. Two-dimensional halide perovskite nanomaterials and heterostructures. *Chem. Soc. Rev.* **2018**, *47*, 6046−6072.
(37) Pospischil, A.; Furchi, M. M.; Mueller, T. Solar-energy conversion and light emission in an atomic monolayer p-n diode. *Nat. Nanotechnol.* **2014**, *9*, 257−261.
(38) Poli, I.; Eslava, S.; Cameron, P. Tetrabutylammonium cations for moisture-resistant and semitransparent perovskite solar cells. *J. Mater. Chem. A* **2017**, *5*, 22325−22333.
(39) Singh, S.; Sharma, B.; Banappanavar, G.; Dey, A.; Chakraborty, S.; Narasimhan, K. L.; Bhargava, P.; Kabra, D. Investigation on Organic Molecule Additive for Moisture Stability and Defect Passivation via Physisorption in $CH_3NH_3PbI_3$ Based Perovskite. *ACS Appl. Energy Mater.* **2018**, *1*, 1870−1877.
(40) Szabó, D.; Mohl, J.; Bálint, A.-M.; Bodor, A.; Rábai, J. Novel generation ponytails in fluorous chemistry: Syntheses of primary, secondary, and tertiary (nonafluoro-tert-butyloxy)ethyl amines. *J. Fluorine Chem.* **2006**, *127*, 1496−1504.
(41) Chen, Y.; Sun, Y.; Peng, J.; Zhang, W.; Su, X.; Zheng, K.; Pullerits, T.; Liang, Z. Tailoring Organic Cation of 2D Air-Stable Organometal Halide Perovskites for Highly Efficient Planar Solar Cells. *Adv. Energy Mater.* **2017**, *7*, 1700162−1700169.
(42) Konstantakou, M.; Perganti, D.; Falaras, P.; Stergiopoulos, T. Anti-Solvent Crystallization Strategies for Highly Efficient Perovskite Solar Cells. *Crystals* **2017**, *7*, 291−312.
(43) Jeon, N. J.; Noh, J. H.; Kim, Y. C.; Yang, W. S.; Ryu, S.; Seok, S. I. Solvent engineering for high-performance inorganic-organic hybrid perovskite solar cells. *Nat. Mater.* **2014**, *13*, 897−903.
(44) Mao, L.; Tsai, H.; Nie, W.; Ma, L.; Im, J.; Stoumpos, C. C.; Malliakas, C. D.; Hao, F.; Wasielewski, M. R.; Mohite, A. D.; Kanatzidis, M. G. Role of Organic Counterion in Lead- and Tin-Based Two-Dimensional Semiconducting Iodide Perovskites and Application in Planar Solar Cells. *Chem. Mater.* **2016**, *28*, 7781−7792.
(45) Mousdis, G. A.; Papavassiliou, G. C.; Raptopoulou, C. P.; Terzis, A. Preparation and characterization of $[H_3N(CH_2)_6NH_3]PbI_4$ and similar compounds with a layered perovskite structure. *J. Mater. Chem.* **2000**, *10*, 515−518.
(46) Muljarov, E. A.; Tikhodeev, S. G.; Gippius, N. A.; Ishihara, T. Excitons in self-organized semiconductor/insulator superlattices: PbI-based perovskite compounds. *Phys. Rev. B: Condens. Matter Mater. Phys.* **1995**, *51*, 14370−14378.
(47) Giannozzi, P.; Baroni, S.; Bonini, N.; Calandra, M.; Car, R.; Cavazzoni, C.; Ceresoli, D.; Chiarotti, G. L.; Coccioni, M.; Dabo, I.; Dal Corso, A.; de Gironcoli, S.; Fabris, S.; Fratesi, G.; Gebauer, R.; Gerstmann, U.; Gougoussis, C.; Kokalj, A.; Lazzeri, M.; Martin-Samos, L.; Marzari, N.; Mauri, F.; Mazzarello, R.; Paolini, S.; Pasquarello, A.; Paulatto, L.; Sbraccia, C.; Scandolo, S.; Sclauzero, G.; Seitsonen, A. P.; Smogunov, A.; Umari, P.; Wentzcovitch, R. M.

DOI: 10.1021/acs.chemmater.8b03377
Chem. Mater. 2018, 30, 8211−8220

Quantum Espresso: a modular and open-source software project for quantum simulations of materials. *J. Phys.: Condens. Matter* **2009**, *21*, 395502−395521.
(48) Fraccarollo, A.; Cantatore, V.; Boschetto, G.; Marchese, L.; Cossi, M. Ab initio modeling of 2D layered organohalide lead perovskites. *J. Chem. Phys.* **2016**, *144*, 164701−164714.
(49) Fraccarollo, A.; Canti, L.; Marchese, L.; Cossi, M. First principles study of 2D layered organohalide tin perovskites. *J. Chem. Phys.* **2017**, *146*, 234703−234713.
(50) Even, J.; Pedesseau, L.; Jancu, J.-M.; Katan, C. Importance of Spin−Orbit Coupling in Hybrid Organic/Inorganic Perovskites for Photovoltaic Applications. *J. Phys. Chem. Lett.* **2013**, *4*, 2999−3005.
(51) Umari, P.; Mosconi, E.; De Angelis, F. Relativistic GW calculations on $CH_3NH_3PbI_3$ and $CH_3NH_3SnI_3$ Perovskites for Solar Cell Applications. *Sci. Rep.* **2015**, *4*, 4467−4474.
(52) Menéndez-Proupin, E.; Palacios, P.; Wahnón, P.; Conesa, J. C. Self-consistent relativistic band structure of the $CH_3NH_3PbI_3$ perovskite. *Phys. Rev. B: Condens. Matter Mater. Phys.* **2014**, *90*, 045207−045214.
(53) Gauthron, K.; Lauret, J. S.; Doyennette, L.; Lanty, G.; Al Choueiry, A.; Zhang, S. J.; Brehier, A.; Largeau, L.; Mauguin, O.; Bloch, J.; Deleporte, E. Optical spectroscopy of two-dimensional layered $(C_6H_5C_2H_4\text{-}NH_3)_2\text{-}PbI_4$ perovskite. *Opt. Express* **2010**, *18*, 5912−5919.
(54) Kawano, N.; Koshimizu, M.; Sun, Y.; Yahaba, N.; Fujimoto, Y.; Yanagida, T.; Asai, K. Effects of Organic Moieties on Luminescence Properties of Organic−Inorganic Layered Perovskite-Type Compounds. *J. Phys. Chem. C* **2014**, *118*, 9101−9106.
(55) Kamminga, M. E.; Fang, H.-H.; Filip, M. R.; Giustino, F.; Baas, J.; Blake, G. R.; Loi, M. A.; Palstra, T. T. M. Confinement Effects in Low-Dimensional Lead Iodide Perovskite Hybrids. *Chem. Mater.* **2016**, *28*, 4554−4562.
(56) Williams, R. T.; Song, K. S. The self-trapped exciton. *J. Phys. Chem. Solids* **1990**, *51*, 679−716.
(57) Booker, E. P.; Thomas, T. H.; Quarti, C.; Stanton, M. R.; Cameron, D.; Dashwood, C. D.; Gillett, A. J.; Richter, J. M.; Pearson, A. J.; Davis, N. J. L. K.; Sirringhaus, H.; Price, M. B.; Greenham, N. C.; Beljonne, D.; Dutton, S. E.; Deschler, F. Formation of Long-Lived Color Centers for Broadband Visible Light Emission in Low-Dimensional Layered Perovskites. *J. Am. Chem. Soc.* **2017**, *139*, 18632−18639.
(58) Zhang, S.; Lanty, G.; Lauret, J.-S.; Deleporte, E.; Audebert, P.; Galmice, L. Synthesis and optical properties of novel organic−inorganic hybrid nanolayer structure semiconductors. *Acta Mater.* **2009**, *57*, 3301−3309.
(59) Smith, M. D.; Jaffe, A.; Dohner, E. R.; Lindenberg, A. M.; Karunadasa, H. I. Structural origins of broadband emission from layered Pb−Br hybrid perovskites. *Chem. Sci.* **2017**, *8*, 4497−4504.
(60) Marques, M. A. L.; Maitra, N. T.; Nogueira, F. M. S.; Gross, E. K. U.; Rubio, A. *Fundamentals of Time-Dependent Density Functional Theory*; Springer-Verlag: Berlin, 2012.
(61) Umari, P.; Pasquarello, A. *Ab initio* Molecular Dynamics in a Finite Homogeneous Electric Field. *Phys. Rev. Lett.* **2002**, *89*, 157602−157606.
(62) Umari, P.; Mosconi, E.; De Angelis, F. Infrared Dielectric Screening Determines the Low Exciton Binding Energy of Metal-Halide Perovskites. *J. Phys. Chem. Lett.* **2018**, *9*, 620−627.
(63) Stroppa, A.; Di Sante, D.; Barone, P.; Bokdam, M.; Kresse, G.; Franchini, C.; Whangbo, M.-H.; Picozzi, S. Tunable ferroelectric polarization and its interplay with spin−orbit coupling in tin iodide perovskites. *Nat. Commun.* **2014**, *5*, 5900−5908.
(64) Quarti, C.; Mosconi, E.; De Angelis, F. Interplay of Orientational Order and Electronic Structure in Methylammonium Lead Iodide: Implications for Solar Cell Operation. *Chem. Mater.* **2014**, *26*, 6557−6569.
(65) Li, Z. Q.; Podzorov, V.; Sai, N.; Martin, M. C.; Gershenson, M. E.; Di Ventra, M.; Basov, D. N. Light Quasiparticles Dominate Electronic Transport in Molecular Crystal Field-Effect Transistors. *Phys. Rev. Lett.* **2007**, *99*, 016403−016416.
(66) Li, Y.; Yi, Y.; Coropceanu, V.; Brédas, J.-L. Optical conductivity and optical effective mass in a high-mobility organic semiconductor: Implications for the nature of charge transport. *Phys. Rev. B: Condens. Matter Mater. Phys.* **2004**, *90*, 245112−245120.
(67) Dalvi, V. H.; Rossky, P. Molecular origins of fluorocarbon hydrophobicity. *Proc. Natl. Acad. Sci. U. S. A.* **2010**, *107*, 13603−13610.
(68) Decato, S.; Bemis, T.; Madsen, E.; Mecozzi, S. Synthesis and characterization of perfluoro-tert-butyl semifluorinated amphiphilic polymers and their potential application in hydrophobic drug delivery. *Polym. Chem.* **2014**, *5*, 6461−6471.
(69) Kolomiets, E.; Buhler, E.; Candau, S. J.; Lehn, J.-M. Structure and Properties of Supramolecular Polymers Generated from Heterocomplementary Monomers Linked through Sextuple Hydrogen-Bonding Arrays. *Macromolecules* **2006**, *39*, 1173−1181.
(70) Xiao, X.; Antony, S.; Kohlhagen, G.; Pommier, Y.; Cushman, M. Design, synthesis, and biological evaluation of cytotoxic 11-aminoalkenylindenoisoquinoline and 11-diaminoalkenylindenoisoquinoline topoisomerase I inhibitors. *Bioorg. Med. Chem.* **2004**, *12*, 5147−5160.
(71) Varala, R.; Adapa, S. R. Novel Approach to the Synthesis of (R,S)-Baclofen via PD(II)-Bipyridine−Catalyzed Conjugative Addition. *Synth. Commun.* **2006**, *36*, 3743−3746.
(72) Laurent, Ph.; Blancou, H.; Commeyras, A. Synthèse de diamines à chaînes perfluoroalkylées. *J. Fluorine Chem.* **1993**, *62*, 173−182.

DOI: 10.1021/acs.chemmater.8b03377
Chem. Mater. 2018, 30, 8211−8220